Supporting Information

On the microscopic origin of Soret coefficient minima in liquid mixtures

Oliver R. Gittus and Fernando Bresme

Department of Chemistry, Molecular Sciences Research Hub,
Imperial College London,
London W12 0BZ, United Kingdom.

Contents

1 Additional results & discussion

1.1 Equation of state and phase diagram

Fig. 1(a) shows the equation of state of the mixture as a function of x_1. The equilibrium-NPT and NEMD results are in excellent agreement, indicating that the local equilibrium hypothesis is fulfilled in the NEMD simulations. The mixture is expected to have a solid-solution phase diagram,[1] and the thermodynamically stable phase for $x_1 = 0$ is a solid (see Sec. 2.9 below). Therefore, the mixture crosses three regions of the phase diagram along the (x_1; $P = 0.46 \ \epsilon\sigma^{-3}$, $T = 0.62 \ \epsilon k_{\mathrm{B}}^{-1}$) line: a liquid-liquid mixture for $x_l < x_1 < 1$ where x_l corresponds to the liquidus; a liquid-solid coexistence region $x_s \leq x_1 \leq x_l$ where x_s corresponds to the solidus; and a solid-solid mixture for $0 < x_1 < x_s$. All the results presented in this work correspond to a liquid-liquid mixture, including $x_1 \leq x_l$ for which our simulations are of the metastable supercooled liquid-liquid mixture. Thus, it is necessary to estimate x_l in order to gauge the range of validity of our results.

For an ideal solution the phase diagram can be estimated using the equations[2,3]

$$\ln \frac{x_{s,1}}{x_{l,1}} = \frac{\Delta H_{\mathrm{fus},1}}{R} \left(\frac{1}{T_{m,1}} - \frac{1}{T} \right) \tag{1}$$
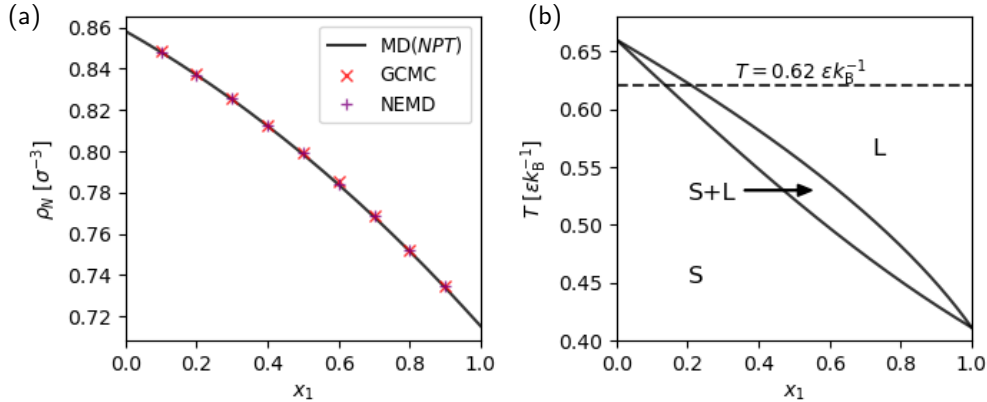
Figure 1: Equation of state and phase diagram of the LJ mixture. (a) The number density ρ_N for ($P = 0.46 \ \epsilon\sigma^{-3}$, $T = 0.62 \ \epsilon k_{\mathrm{B}}^{-1}$) as a function of mole fraction x_1, as predicted by MD(NPT), GCMC and NEMD simulations. All simulated systems correspond to a liquid, which is metastable for $x_1 \leq x_l$, where x_l is the mole fraction of the liquidus shown in (b). (b) The estimated solid solution phase diagram of the mixture at $P = 0.46 \ \epsilon\sigma^{-3}$. The symbols are: S = solid solution; L = liquid mixture; S+L = solid and liquid coexistence.

$$\ln \frac{1 - x_{s,1}}{1 - x_{l,1}} = \frac{\Delta H_{\mathrm{fus},2}}{R} \left(\frac{1}{T_{m,2}} - \frac{1}{T} \right) \tag{2}$$

where R is the gas constant; $T_{m,i}$ and $\Delta H_{\mathrm{fus},i}$ are the melting temperature and enthalpy of fusion, respectively, of species i; and $x_{l,1}$ and $x_{s,1}$ are the mole fractions of the liquidus and solidus for end-member 1. Eqs. 1&2 further assume that there is no difference in isobaric heat capacity between the supercooled liquid and pure solid of species 1 at T.[3] The predicted phase diagram is shown in Fig. 1(b), with $x_l \approx 0.21$ at $T = 0.62\ \epsilon k_{\mathrm{B}}^{-1}$. The mixture is near-ideal at $x_1 \approx 0.21$ with thermodynamic factor $\Gamma \approx 0.8$, and the assumption of ideal mixing is therefore expected to be a good approximation. The S_T and Γ minima at $x_1 \sim 0.5$ (see the main text) are safely within the liquid-liquid mixture region of the phase diagram.

1.2   Ideal and excess contributions to the thermodynamic factor
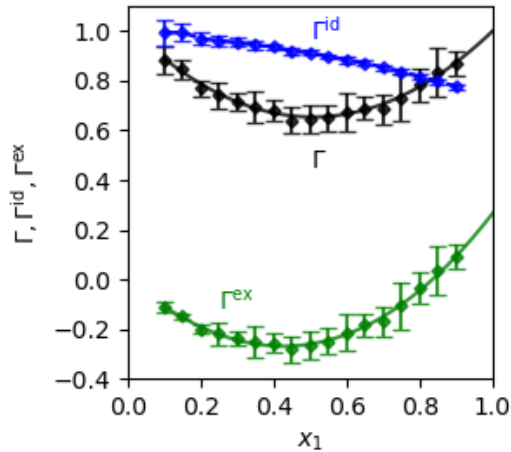

Figure 2: The thermodynamic factor Γ, and its ideal Γ^{id} and excess Γ^{ex} contributions, as a function of mole fraction x_1. All results correspond to the FEP data.

We split Γ into its excess and ideal gas contributions, Γ^{ex} and Γ^{id} respectively (Fig. 2). $\Gamma^{\mathrm{id}} = x_1 (\partial \mu_1^{\mathrm{id}}/\partial x_1)_{P,T}/(k_B T) = (x_1/\rho_N)(\partial \rho_N/\partial x_1)_{P,T} + 1$ depends only on x_1, the total number density ρ_N and its derivative, while $\Gamma^{\mathrm{ex}} = x_1 (\partial \mu_1^{\mathrm{ex}}/\partial x_1)_{P,T}/(k_B T)$ depends on the excess chemical potential μ_1^{ex} and therefore the inter-particle interactions in the system. Γ^{id} monotonically decreases with increasing x_1, while Γ^{ex} possesses a minimum at $x_1^{\min(\Gamma^{\mathrm{ex}})} = 0.4 \pm 0.1$ as determined by fitting a cubic function. Thus, the minimum arises through Γ^{ex}, although its position is shifted by ~ 0.1 (to $x_1 \sim 0.5$) due to the Γ^{id} contribution.

1.3 Theoretical models

We calculate the Soret coefficient according to the models of Haase[4,5] (S_T^{H}), Kempers[5] (S_T^{K}) Shukla and Firoozabadi[6] (S_T^{SF}), and Artola, Rousseau and Galliéro[7] (S_T^{ARG}):

$$TS_{T,1}^{\mathrm{H}} = \frac{m_1 m_2}{m_1 x_1 + m_2 x_2}\frac{(h_2 - h_2^0)/m_2 - (h_1 - h_1^0)/m_1}{x_1(\partial\mu_1/\partial x_1)_{P,T}} + \frac{RT^2}{x_1(\partial\mu_1/\partial x_1)_{P,T}}S_T^0 \tag{3}$$

$$TS_{T,1}^{\mathrm{K}} = \frac{v_1 v_2}{v_1 x_1 + v_2 x_2}\frac{(h_2 - h_2^0)/v_2 - (h_1 - h_1^0)/v_1}{x_1(\partial\mu_1/\partial x_1)_{P,T}} + \frac{RT^2}{x_1(\partial\mu_1/\partial x_1)_{P,T}}S_T^0 \tag{4}$$

$$TS_{T,1}^{\mathrm{SF}} = \frac{u_1/\tau_1 - u_2/\tau_2}{x_1(\partial\mu_1/\partial x_1)_{P,T}} + \frac{(v_2 - v_1)(x_1 u_1/\tau_1 + x_2 u_2/\tau_2)}{(x_1 v_1 + x_2 v_2)x_1(\partial\mu_1/\partial x_1)_{P,T}} \tag{5}$$

$$TS_{T,1}^{\mathrm{ARG}} = \frac{\Delta G_2^{\ddagger} - \Delta G_1^{\ddagger}}{RT} + \frac{m_2 - m_1}{m_2 + m_1}\frac{\Delta G_2^{\ddagger} + \Delta G_1^{\ddagger}}{RT} \tag{6}$$

where h_i, u_i and v_i are the partial molar enthalpy, internal energy and volume of species $i = 1, 2$. R is the gas constant. The Kempers model was derived by considering a non-isothermal two-bulb system, with the main assumption that the stationary state is the macroscopic state with the maximum number of microstates. Within this model, S_T^{K} corresponds to the centre-of-volume frame of reference, while Haase's earlier educated guess S_T^{H} can be derived in the centre-of-mass frame.[5] h_i^0 and S_T^0 correspond to an ideal gas state at the same temperature (calculated from kinetic theory), and capture the kinetic contribution to S_T. The Shukla-Firoozabadi model was developed with its origins in linear non-equilibrium thermodynamics (LNET), along the same lines as earlier models[8,9] that all correlate the net heat of transport with the activation energy for viscous flow $\Delta U_\eta^{\ddagger}$. The parameter $\tau_i = \Delta U_{c,i}/\Delta U_{\eta,i}^{\ddagger}$, where ΔU_c is the cohesive energy, is related to the size of the hole required for viscous flow (from the hole theory of liquids), and is often treated as an adjustable parameter. The Artola-Rousseau-Galliéro model is Prigogine's model (S_T^{P}) modified to include the mass contribution; for $m_1 = m_2$ it reduces to $S_{T,1}^{\mathrm{ARG}} = S_{T,1}^{\mathrm{P}} = (\Delta G_2^{\ddagger} - \Delta G_1^{\ddagger})/RT^2$. In these two kinetic models, thermal diffusion is described as a coupled diffusion-activated process, for which the elementary process can be summarized as a swap between two particles of different species along a temperature gradient. The activation energies $\Delta G_i^{\ddagger}$ were calculated from $D_i = D_i^0 \exp\left(-\Delta G_i^{\ddagger}/RT\right)$ (see Fig. 3), where D_i^0 is a constant and the self-diffusion coefficients D_i have been corrected for finite-size effects (see Sec. 2.6 below). The molecular motion of a component through the mixture is better identified with self-diffusion rather than viscous flow; the use of the latter was historically motivated by the scarcity of self-diffusion data, even for pure components, and justified by the similar activation energies expected from Eyring's rate theory applied to liquids.[10] By using self-diffusion data, the Artola-Rousseau-Galliéro model represents a step forward in the modelling of thermal diffusion.
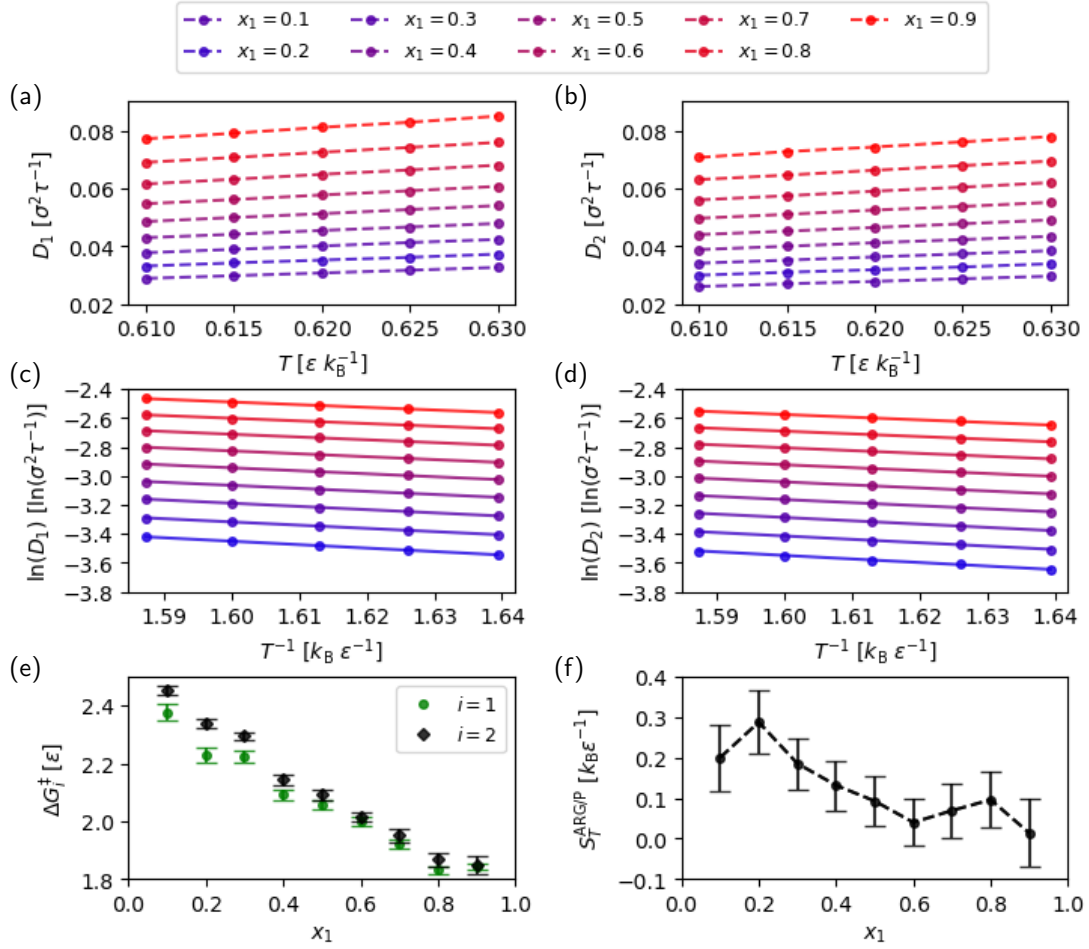
Figure 3: The Soret coefficient predicted by the Artola-Rousseau-Galliéro and Prigogine models, $S_T^{\mathrm{ARG/P}}$, and related quantities. The self-diffusion coefficients D_i as a function of temperature T for species (a) $i = 1$ and (b) $i = 2$. $\ln D_i$ vs. T^{-1} for species (c) $i = 1$ and (d) $i = 2$; the solid lines show linear fits to $\ln D_i = \ln D_i^0 - \Delta G_i^{\ddagger}/(k_B T)$. (e) The activation energies $\Delta G_i^{\ddagger}$ and (e) $S_T^{\mathrm{ARG/P}}$ as a function of mole fraction x_1. Where error bars have not been shown, uncertainties are smaller than the size of the symbols.

A relevant question for the Shukla-Firoozabadi model is how to best estimate the parameters τ_i. Different methods have been proposed, with varying levels of approximations.[6,11–14] The most crude but still a widely adopted[15,16] approach is to set $\tau_1 = \tau_2 = 4.0$ or 3.5, stemming from the observation[6] that $\Delta U_{\mathrm{vap}}/\Delta U_\eta^{\ddagger} = 3\text{-}4$ for many non-associating liquids under normal boiling point conditions, where ΔU_{vap} is the energy of vaporization (ΔU_{vap} is an approximation
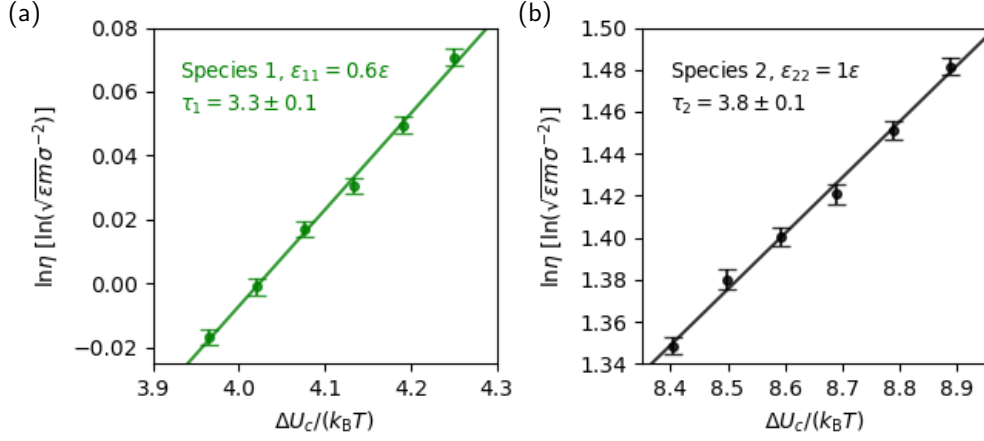
6

Figure 4: $\ln(\eta_i)$ *vs.* $\Delta U_c/(k_B T)$, where η_i and ΔU_c are the shear viscosity and cohesive energy of a pure liquid of species $i = 1, 2$. (a) Species 1 and (b) species 2. The solid lines show linear fits to $\ln \eta_i = \ln A + U_c/(\tau_i k_B T)$. The data points correspond to $P = 0.46 \epsilon \sigma^{-3}$ and $T/(\epsilon k_B^{-1}) = 0.605$, 0.61, 0.615, 0.62, 0.625 and 0.63.

to ΔU_c). While permissible for some mixtures, this approach is unsuitable for others and has been criticised.[11,13,14] In this work, we use the method originally proposed[6], but not employed, by Shukla and Firoozabadi with the caveat that they used the approximation $\Delta U_{\mathrm{vap}} \approx \Delta U_c$. As shown in Fig. 4, we calculate τ_i of the pure components from $\eta_i = A \exp\left(\Delta U_{\eta,i}^{\ddagger}/RT\right) = A \exp\left(\Delta U_{c,i}/\tau_i RT\right)$, where η_i is the shear viscosity, to give $(\tau_1, \tau_2) = (3.3 \pm 0.1, 3.8 \pm 0.1)$, and use these τ_i for the entire composition range. This approach does not account for the composition dependence of τ_i.
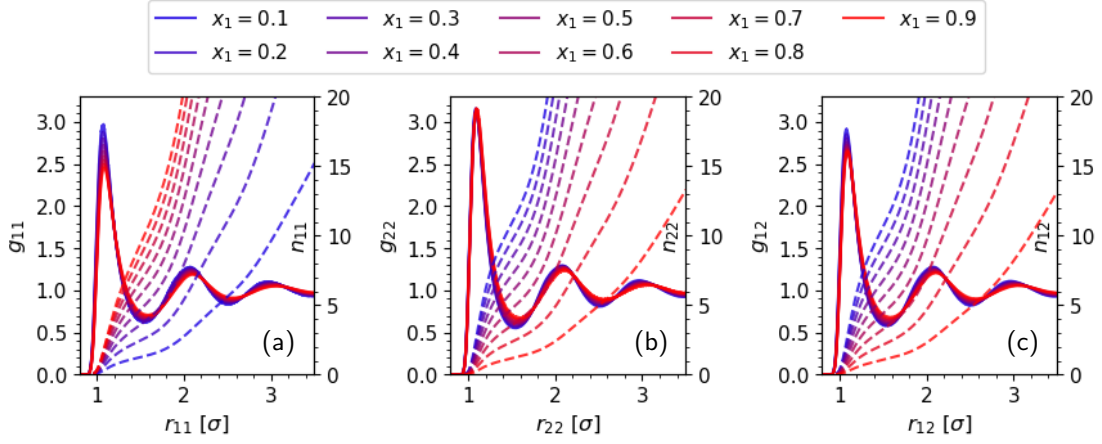
1.4 Radial distribution functions

Figure 5: Radial distribution functions g_{ij} and coordination number n_{ij} of the Lennard-Jones mixtures: (a) g_{11} and n_{11}; (b) g_{22} and n_{22}; (c) g_{12} and n_{12}. r_{ij} is the radial distance between species i and j. Solid lines show g_{ij} (left axis) and the dashed lines show n_{ij} (right axis).

1.5 Thermal conductivity

It is well established that the Soret effect reduces the thermal conductivity of the mixture.[17] From LNET, the thermal conductivity λ is given in terms of the phenomenological coefficients $L_{\alpha\beta}$ and $L'_{\alpha\beta}$ as

$$\lambda = \frac{1}{T^2}\left(L_{qq} - \frac{L_{1q}L_{q1}}{L_{11}}\right) = \frac{1}{T^2}\left(L'_{qq} - \frac{L'_{1q}L'_{q1}}{L_{11}}\right) \tag{7}$$

where the enthalpic terms in the primed coefficients cancel exactly to give the same thermal conductivity as for the unprimed coefficients. λ can therefore be split into two contributions: (1) the thermal conductivity in the absence of coupling effects, $\lambda_0 = L_{qq}/T^2$ or $\lambda'_0 = L'_{qq}/T^2$, and (2) the mass-heat coupling term, $\delta\lambda = -L_{1q}L_{q1}/(L_{11}T^2)$ or $\delta\lambda' = -L'_{1q}L'_{q1}/(L_{11}T^2)$, such that $\lambda = \lambda_0 + \delta\lambda = \lambda'_0 + \delta\lambda'$. The Soret effect should always decrease λ, and thus $\lambda = \lambda_0 - |\delta\lambda| = \lambda'_0 - |\delta\lambda'|$.

We show in Fig. 6 the thermal conductivity of the mixture, and the contribution due to heat-mass coupling. The thermal conductivities calculated via NEMD and equilibrium-MD (EMD) are in excellent agreement. The thermal conductivity of the mixture decreases with increasing x_1. λ increases with density, consistent with the trend observed for simple fluids, including LJ fluids, along an isotherm. However, the density dependence of the mixture slightly deviates from the
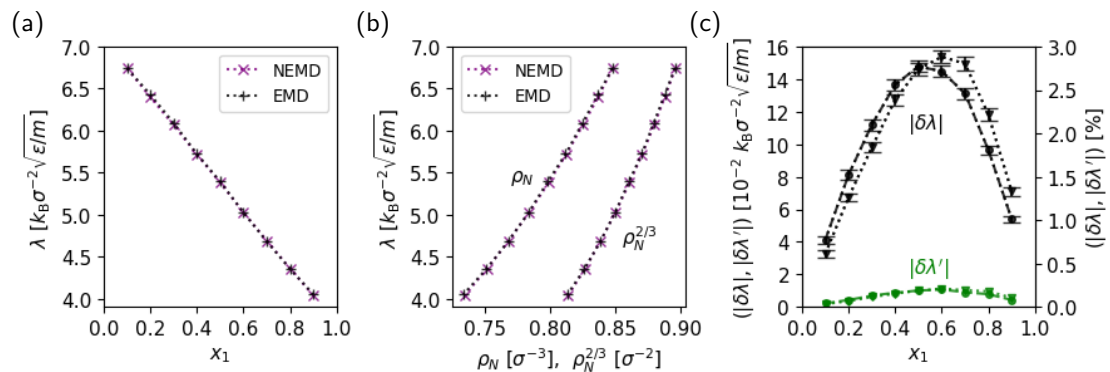
Figure 6: Thermal conductivity λ of the Lennard-Jones mixture. λ as a function of (a) mole fraction x_1 and (b) number density ρ_N as well as $\rho_N^{2/3}$. (c) The decrease in λ due to heat-mass coupling, $|\delta\lambda|$ and $\delta\lambda'$. In (c), circles with dashed lines (--○--) show the absolute values (left axis) and downward triangles with dotted lines ($\cdot\cdot\nabla\cdot\cdot$) show the values as a percentage of λ (right axis). Where error bars have not been shown, uncertainties are smaller than the size of the symbols.

$\lambda \propto \rho_N^{2/3}$ scaling reported[18] for pure LJ fluids. The $|\delta\lambda|$ and $|\delta\lambda'|$ terms both feature a maximum, which is a direct consequence of the minimum in S_T and Γ (indeed, $\delta\lambda' = -L'_{1q}S_T\Gamma k_B/m_1$ for $m_1 = m_2$). $|\delta\lambda|$ amounts to a reduction of ~1-3% relative to λ for $0.1 \leq x_1 \leq 0.9$, while $|\delta\lambda'|$ is an order of magnitude smaller with values from 0 to 0.3%. The result that heat-mass coupling reduces the thermal conductivity by at most a few percent is consistent with previous studies[19] examining different LJ mixtures.

2 Physical properties from simulations

All simulations were performed using the software package LAMMPS[20] (v. 3 March 2020).

2.1 Equilibrium molecular dynamics simulations

Equilibrium molecular dynamics (EMD) simulations of the mixture were performed in the NPT, NVT and NVE ensembles, targeting various thermodynamic states. Unless stated otherwise (i.e. for the finite-size analyses) a cubic simulation cell containing 5000 particles was used. A timestep of 0.002τ was used for the NPT and NVT simulations. For the NPT and NVT simulations, temperature was controlled by the Nosé-Hoover chain thermostat, with 3 chains, and a time constant of $1\ \tau$. Additionally in the NPT simulations, pressure was controlled using a Nosé-Hoover chain barostat, also with 3 chains, and a time constant of $4\ \tau$. For the NPT simulations, a single replica was performed for each $(x_1,\ P,\ T)$ state point, consisting of at least $2 \times 10^4\ \tau$ of equilibration, followed by a $1\text{-}2\times10^5\ \tau$ production run. For the NVT simulations, sampling consisted of 20-200 replicas for each $(x_1,\ \rho,\ T)$ state point depending on the system size, which varied from $N = 1000\text{-}120,000$ particles; each replica was equilibrated for $2 \times 10^3\ \tau$ followed by $10^4\ \tau$ of production. The exceptions to this were the large $N = 0.5\text{-}5 \times 10^6$ systems simulated for the KBIs (Sec. 2.8 below), which had both equilibration and production times of $10^3\tau$.

Simulations in the NVE ensemble targeted different compositions along the ($P = 0.46\ \epsilon\sigma^{-3}$, $T = 0.62\ \epsilon k_{\mathrm{B}}^{-1}$) isobar-isotherm. For each state point, replicas were first spawned from NVT simulations and monitored for an initial $2 \times 10^3\ \tau$. If the average temperature was within $\pm0.0005\ \epsilon k_{\mathrm{B}}^{-1}$ of $T = 0.62\ \epsilon k_{\mathrm{B}}^{-1}$, the replica was continued for a further $2 \times 10^4\ \tau$ of production. Replicas were also subsequently started from these successful NVE trajectories. A total of 50-100 statistically independent replicas were performed for each state point, all of which had an average temperature $\langle T \rangle_{NVE}$ within $\pm0.0005\ \epsilon k_{\mathrm{B}}^{-1}$ of the target temperature. A smaller timestep of $\delta t = 0.001\ \tau$ was used to improve energy conservation (reduce temperature drift) and therefore increase the sampling times available in the small $\pm0.0005\ \epsilon k_{\mathrm{B}}^{-1}$ temperature window, and also to reduce the discretization error for the numerical integration of correlation functions (see secs. 2.4 & 2.6 below).

2.2 Soret coefficient and thermal conductivity from NEMD

2.2.1 Simulation details

The Soret coefficient S_T and thermal conductivity λ were calculated from boundary-driven non-equilibrium molecular dynamics simulations (NEMD) in the stationary state. An elongated (tetragonal) simulation cell of dimensions $(L_x, L_y, L_z) = (20, 20, 30)\sigma$ was used, with 3D periodic boundary conditions. Two thermostatting regions, hot and cold, were located in the centre and edges of the simulation, respectively (see Fig. 7). The thermostatting regions had a width $\Delta z = 3\sigma$ and extended over the entire (x, y) plane, such that the temperature gradients were generated along the z-direction. For the thermostatting procedure, a simple velocity rescaling algorithm was used to maintain the hot and cold thermostatting regions at temperatures T_h and T_c, respectively. The velocities of all particles in each region were rescaled, every timestep, by a factor $\alpha = \sqrt{K_t/K_c}$ where K_t and K_c are the target and current kinetic energies of the region. This velocity rescaling procedure does not conserve linear momentum, so the system's centre-of-mass velocity was subtracted from each particle at every time step in order to ensure linear momentum conservation. A timestep of $\delta t = 0.002\ \tau$ was used.

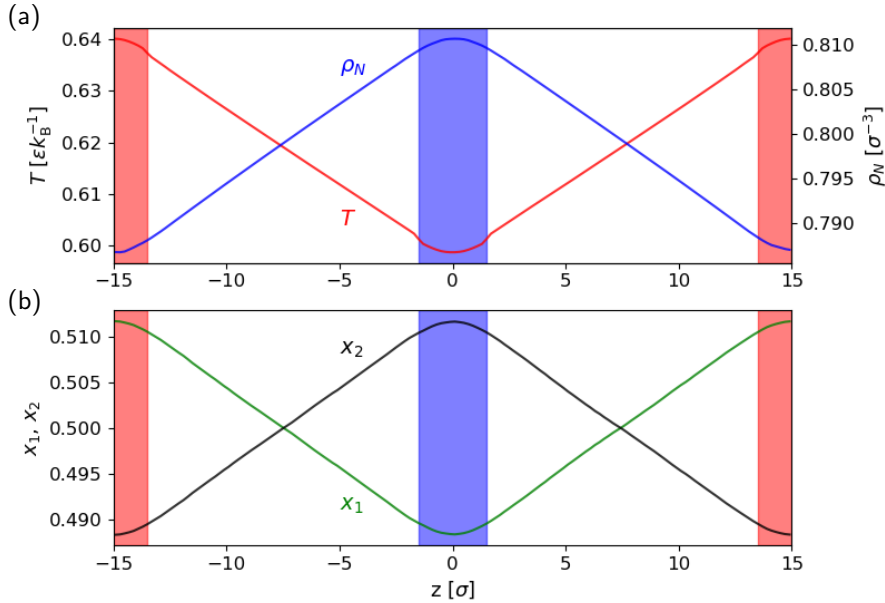Figure 7: Representative (a) temperature T and number density ρ_N profiles, and (b) mole fraction, x_1 and x_2, profiles for the NEMD simulations. The blue (cold) and red (hot) indicate the location of the thermostatting regions in the simulation cell.

For each system, the average density, mole fraction and thermostat temperatures were chosen to give $\langle P_{zz} \rangle$ within ± 0.001 $\epsilon\sigma^{-3}$ of the target pressure $P = 0.46$ $\epsilon\sigma^{-3}$, where P_{zz} is the pressure tensor component parallel to the heat flux vector. Relatively small (by simulation standards) temperature differences $\Delta T = T_h - T_c \approx 0.04$ ϵk_B^{-1} and resulting gradients $\nabla T \approx 2.9 \times 10^{-3}$ $\epsilon k_B^{-1} \sigma^{-1}$ were used to accurately target the thermodynamic state. For each system, 10 statistically independent replicas were generated, each consisting of an initial $2 \times 10^4 \tau$ to establish the stationary state, followed by $2 \times 10^6 \tau$ for data collection.

In the stationary state, this set-up results in two equal but opposite temperature gradients, and therefore in equal and opposite heat fluxes, such that the system is completely periodic. The heat flux across the system, $\boldsymbol{J}_q = (0, 0, \pm J_q)$, can be obtained from the continuity equation

$$J_q = \frac{|\langle \Delta U \rangle|}{2 \delta t A} \tag{8}$$

where $A = L_x \times L_y$ is the cross-sectional area of the simulation cell, δt is the timestep, and ΔU is the internal energy exchanged at each timestep. The employed simple rescaling thermostat only changes the kinetic energy such that $\Delta U = \Delta K$. The factor of 2 in the denominator accounts for the two heat fluxes (equal magnitude and opposite direction) generated in this setup. The thermal conductivity λ was then calculated using Fourier's Law:

$$\boldsymbol{J}_q = -\lambda \nabla T \tag{9}$$

where ∇T is the *local* temperature gradient. The Soret coefficient S_T was calculated using Eq. 1 in the main text, again employing local values of the gradients ∇T and ∇x_1. Local densities ρ, mol fractions x_1 and temperatures T were determined from a 1σ bin close to the centre of each *NVE* compartment. The position of the bin was chosen such that $T = 0.62$ ϵk_B^{-1}. The local values of ∇T and ∇w_1 were determined by fitting straight lines to the temperature and mole fraction profiles within a range of $\pm 2.5\sigma$ around the selected state point.

2.2.2 Linear response

We demonstrate in Fig. 8 that the magnitude of temperature gradients used in this work are within the linear regime. For these additional simulations, production runs of length $1.5 \times 10^6 \tau$ and $10^6 \tau$ were used for the $\nabla T \approx 1.5 \times 10^{-3}$ $\epsilon k_B^{-1} \sigma^{-1}$ and $\nabla T \approx 4.4 \times 10^{-3}$ $\epsilon k_B^{-1} \sigma^{-1}$ systems, respectively. The values for S_T and λ for $x_1 = 0.5, 0.9$ were calculated by fitting to their linear response (Fig. 8).
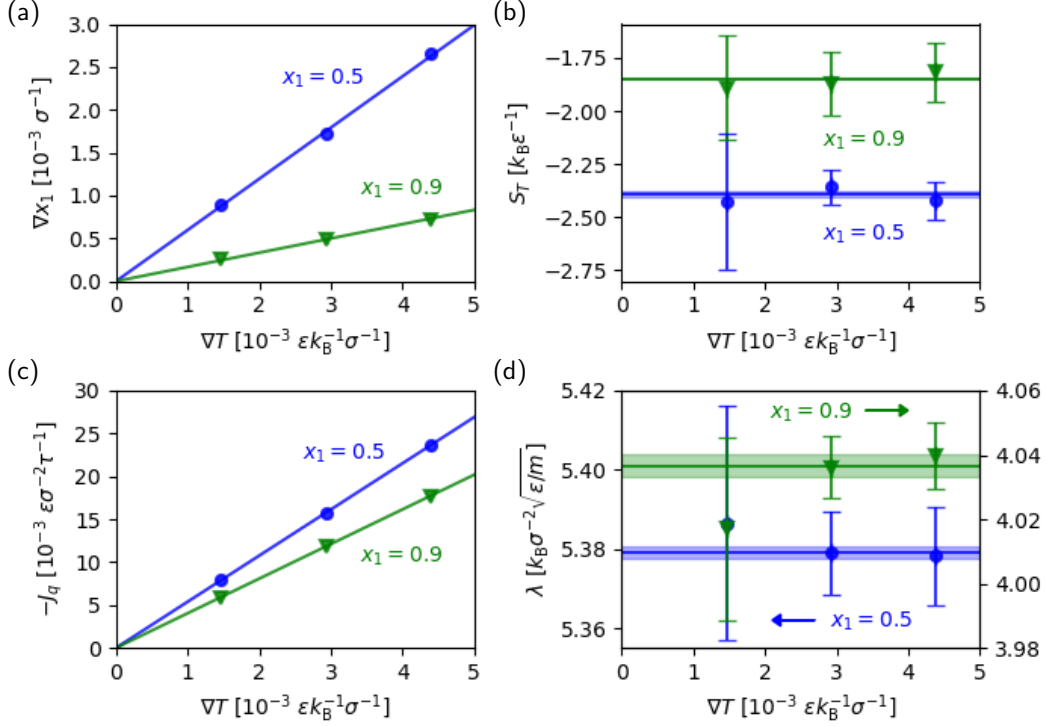
Figure 8: Linear response of the Soret coefficient S_T and thermal conductivity λ: (a) mole fraction gradient ∇x_1, (b) S_T, (c) heat flux J_q and (d) λ as a function of temperature gradient ∇T. The solid lines show fits to $\nabla x_1 = -x_1 x_2 S_T \nabla T$ in (a) and (b), and to Fourier's law $-J_q = \lambda \nabla T$ in (c) and (d). In (a) and (c), statistical uncertainties are smaller than the size of the symbols. In (b) and (d) the shaded areas show the uncertainty associated with the fits.

2.2.3 Finite-size effects

We show in Fig. 9 that the lateral simulation cell length $L_\perp = L_x = L_y$ has a significant effect on S_T. While all but one ($L_\perp/\sigma = 10, 20$ for $x_1 = 0.3$) S_T values agree to within their statistical uncertainties, $|S_T|$ systematically decreases with $L_\perp$: by $\sim$0-10% ($\sim$3-6%) when increasing $L_\perp$ from 10σ to 20σ (20σ to 40σ). Nevertheless, fitting cubic functions to the $L_\perp/\sigma = 10, 20, 40$ data gives $x_1^{\min(S_T)} = 0.5 \pm 0.1$, and further increasing $L_\perp$ is not expected to significantly shift the position of the minimum. Finite-size effects in S_T are expected from those observed in self-diffusion coefficients (Sec. 2.6 below) and D_{12}.[21,22] The impact of finite-size effects on D_T is less well known.

We do not observe appreciable finite-size effects for the thermal conductivity. This is consis-
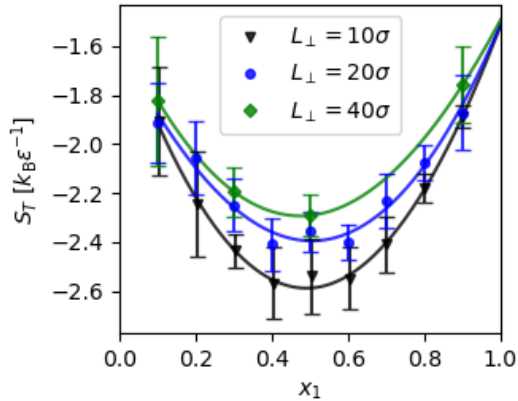
Figure 9: Finite-size effects on the Soret coefficient S_T calculated from NEMD simulations. $L_\perp = L_x = L_y$ is the length of the simulation cell in the direction perpendicular to the heat flux. Solid lines show cubic functions fit to $S_T(x_1)$ where x_1 is the mole fraction of species 1.

tent with the mechanism of thermal transport in molecular liquids (and liquid mixtures), which is dominated by collisions between nearest neighbors, setting a characteristic length scale for heat transport at $\sim 1\sigma$.

The additional simulations for $L_\perp = 10\sigma$ and $L_\perp = 40\sigma$ had production lengths of $4 \times 10^6 \tau$ and $3 \times 10^5 \tau$, respectively.

2.3 Partial molar properties

Partial molar properties z_i were calculated using the equations $z_1 = Z + (1 - x_1)(\partial Z/\partial x_1)_{PTN_2}$ and $z_2 = Z - x_1(\partial Z/\partial x_1)_{PTN_2}$, where Z is the corresponding extensive property. $Z(x_1)$ were calculated from MD simulations in the NPT ensemble. At each selected x_1, two additional simulations were performed at $x_1 \pm 0.01$, and $(\partial Z/\partial x_1)_{PTN_2}$ was then calculated by fitting a straight line through these three points.
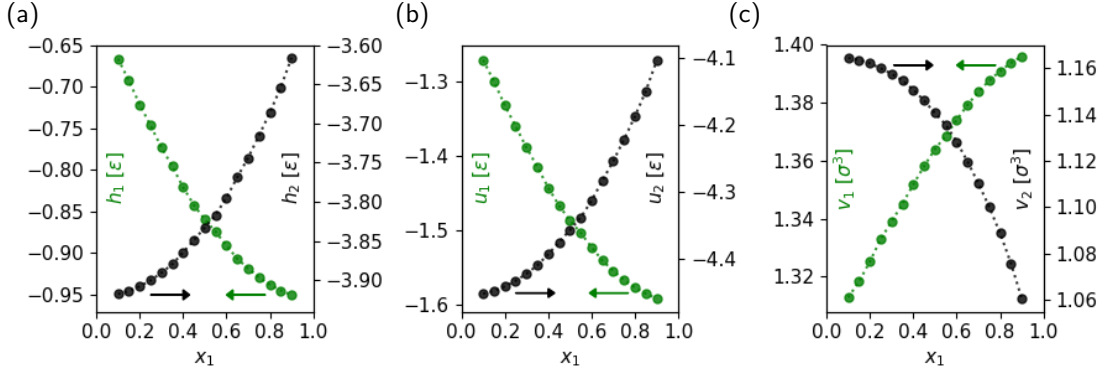
14

Figure 10: Partial molar properties z_i of component $i = 1, 2$ as a function of mole fraction x_1: (a) partial molar enthalpy h_i; (b) partial molar internal energy u_i; and (c) partial molar volume v_i. Statistical uncertainties are smaller or comparable to the size of the symbols.

2.4   Onsager's phenomenological coefficients

The phenomenological coefficients $L_{\alpha\beta}$ were calculated using the Green-Kubo integral formula

$$L_{\alpha\beta} = \frac{V}{3k_{\mathrm{B}}} \lim_{t' \to \infty} \int_0^{t'} \langle \boldsymbol{J}_\alpha(t) \cdot \boldsymbol{J}_\beta(0) \rangle dt \tag{10}$$

where V is the volume of the simulation cell, and the factor of 3 in the denominator averages the contributions from each spatial dimension. In order to calculate L_{qq}, L_{1q}, L_{q1} and L_{11}, the expressions for the heat flux $\boldsymbol{J}_q$ and mass flux $\boldsymbol{J}_1$ in terms of microscopic quantities are required. These are:

$$\boldsymbol{J}_1 = \frac{1}{V} \sum_{i=1}^{N_1} m_i \boldsymbol{v}_i \tag{11}$$

where the sum runs over all N_1 particles of species 1, and in the case of two-body interactions the Irving-Kirkwood formula for heat flux is

$$\boldsymbol{J}_q = \frac{1}{V} \left(\sum_{i=1}^{N} U_i \boldsymbol{v}_i - \sum_{i=1}^{N} \boldsymbol{S}_i \boldsymbol{v}_i \right) = \frac{1}{V} \left(\sum_{i=1}^{N} (\mathcal{V}_i + K_i) \boldsymbol{v}_i - \frac{1}{2} \sum_{i=1}^{N} \sum_{j \neq i}^{N} (\boldsymbol{v}_i \cdot \boldsymbol{F}_{ij}) \boldsymbol{r}_{ij} \right) \tag{12}$$

where U_i is the per-particle internal energy which can be split into potential $\mathcal{V}_i = (1/2) \sum_{j \neq i} u_{ij}(r_{ij})$ and kinetic energy $K_i = (1/2) m_i \boldsymbol{v}_i^2$ contributions; $\boldsymbol{S}_i$ is the per-particle stress tensor; $\boldsymbol{F}_{ij}$ is the force exerted on particle i by particle j; and $\boldsymbol{r}_{ij} = \boldsymbol{r}_j - \boldsymbol{r}_i$ where $\boldsymbol{r}_i$ is the position vector of particle i.

The unprimed coefficients were calculated from simulations in the NVE ensemble. A correlation time of $t_c = 10\tau$ was used for the upper limit of Eq. 10. Selecting this integration limit is a compromise between sampling efficiency and minimizing the resulting truncation error. We show
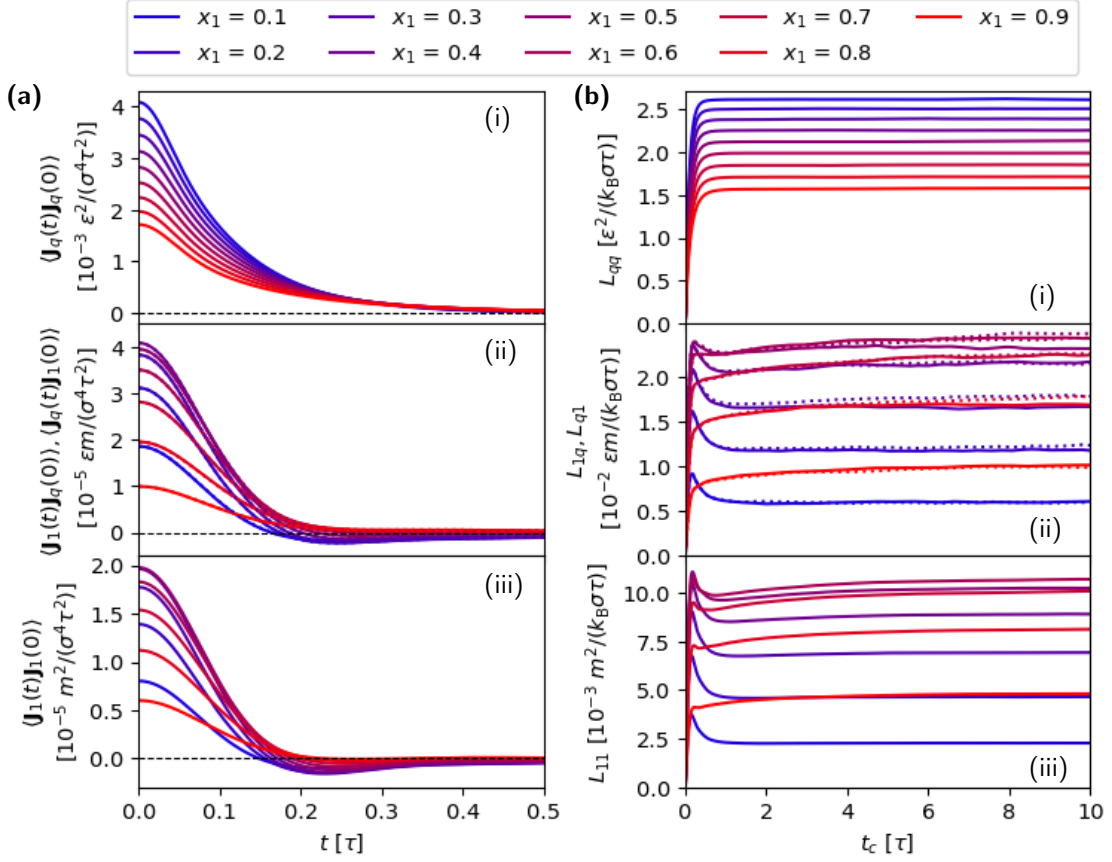
Figure 11: (a) Correlation functions $\langle \boldsymbol{J}_\alpha(t) \cdot \boldsymbol{J}_\beta(0) \rangle$ as a function of time lag t. (b) Convergence of the phenomenological coefficients $L_{\alpha\beta}(t_c)$ with the correlation time t_c used as the upper limit of the integral in Eq. 10. In (a)(ii) and (b)(ii): solid lines show $\langle \boldsymbol{J}_1(t) \cdot \boldsymbol{J}_q(0) \rangle$ and L_{1q}; dotted lines show $\langle \boldsymbol{J}_q(t) \cdot \boldsymbol{J}_1(0) \rangle$ and L_{q1}

in Fig. 11 that $10\,\tau$ is sufficiently long to achieve a well-converged integral, while the exhaustive extent of our sampling is reflected in the associated uncertainty.

The primed coefficients $L'_{\alpha\beta}$ were then obtained from $L_{\alpha\beta}$ using the formulas

$$L'_{qq} = L_{qq} - (L_{1q} + L_{q1})(h_{s,1} - h_{s,2}) + L_{11}(h_{s,1} - h_{s,2})^2 \tag{13}$$

$$L'_{1q} = L_{1q} - L_{11}(h_{s,1} - h_{s,2}) \tag{14}$$

$$L'_{q1} = L_{q1} - L_{11}(h_{s,1} - h_{s,2}) \tag{15}$$

$$L'_{11} = L_{11} \tag{16}$$

16

where $h_{s,i}$ is the specific molar enthalpy of component $i = 1, 2$. These formulas can be derived by comparing expressions for entropy production in LNET, or trivially from the Green-Kubo integral formula (Eq. 10) noting that $\boldsymbol{J}_q' = \boldsymbol{J}_q - (h_{s,1} - h_{s,2})\boldsymbol{J}_1$.[19,23] The difference between $\boldsymbol{J}_q'$ and $\boldsymbol{J}_q$ corresponds to the heat transported due to diffusion.

We show in Fig. 12 the values of coefficients $L_{\alpha\beta}$ and $L'_{\alpha\beta}$. Consistent with Onsager's reciprocal relations, $L'_{1q} = L'_{q1}$ and $L_{1q} = L_{q1}$ to within their associated uncertainties. We therefore average over both reciprocal coefficients to give a single value each for $L'_{1q} = L'_{q1}$ and $L_{1q} = L_{q1}$.
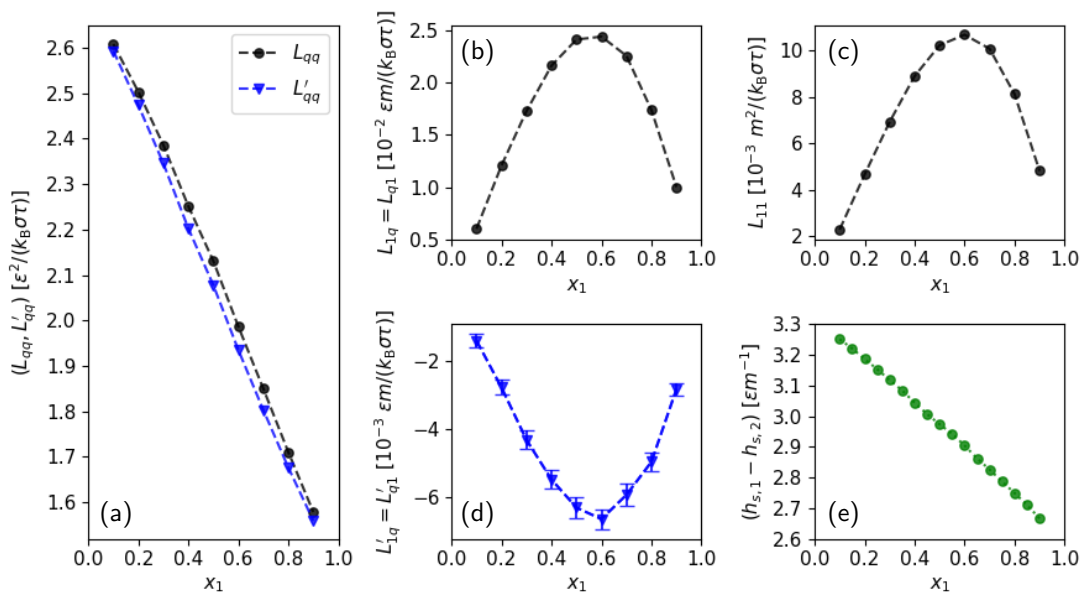

Figure 12: The phenomenological coefficients as a function of the mole fraction x_1: (a) L_{qq} and L'_{qq}; (b) $L_{1q} = L_{q1}$; (c) L_{11}; and (d) $L'_{1q} = L'_{q1}$. (e) The difference in specific partial enthalpies $h_{s,1} - h_{s,2}$, where $h_{s,i}$ is the specific partial enthalpy of component i. Where error bars are not shown, the statistical uncertainty is smaller than the size of the symbol.

2.5 Chemical potentials

The chemical potential of species i was calculated in terms of its ideal (id) and excess (ex) contributions, $\mu_i = \mu_i^{\mathrm{id}} + \mu_i^{\mathrm{ex}}$. The ideal gas contribution μ_i^{id} is given by the formula

$$\mu_i^{\mathrm{id}} = k_B T \ln\left(\rho_{N,i}\Lambda_i^3\right) \tag{17}$$

where $\rho_{N,i} = x_i \rho_N$ and Λ_i are the number density and thermal de Broglie wavelength of species i, respectively. The densities were obtained from MD simulations in the NPT ensemble. By

convention we set $\Lambda_2 = h/\sqrt{2\pi m_2 k_B T} = 1 \Rightarrow \ln(\Lambda_2^3) = 0$ (note that $\Lambda_1 = \Lambda_2$ since $m_1 = m_2$) for $T = 0.62\,\epsilon k_B^{-1}$, and in doing so fix the energy scale by assigning a value to Planck's constant h in Lennard-Jones units. This amounts to a constant shift in μ_i and does not affect $(\partial\mu_i/\partial x_1)_{P,T}$.

The excess chemical potential μ_i^{ex} was calculated from MD simulations at constant T and P using a free energy perturbation (FEP) method. A single particle was inserted into the simulation cell via $(n-1)$ small "steps" along a reversible alchemical thermodynamic path, analogous to slowly "growing" the particle. The Gibbs free energy change for this particle insertion, $\Delta_N^{N+1}G^{\text{ex}}$, is given by

$$\mu_i^{\text{ex}} \approx \Delta_N^{N+1}G^{\text{ex}} = -k_B T \sum_{i=0}^{n-1} \ln \frac{\langle V \exp\left(-\Delta_{\zeta_i}^{\zeta_{i+1}} \mathcal{V}/k_B T\right)\rangle_{\zeta_i}}{\langle V \rangle_{\zeta_i}} \tag{18}$$

where V is the volume of the simulation cell, $\Delta_{\zeta_i}^{\zeta_{i+1}}\mathcal{V}(\zeta, \boldsymbol{r}) = \mathcal{V}_{\zeta_{i+1}}(\zeta, \boldsymbol{r}) - \mathcal{V}_{\zeta_i}(\zeta, \boldsymbol{r})$ and ζ is a coupling parameter that connects the reference (N) and perturbed $(N+1)$ systems according to $\mathcal{V}(\zeta, \boldsymbol{r}) = \zeta \mathcal{V}_{N+1}(\boldsymbol{r}) + (1-\zeta)\mathcal{V}_N(\boldsymbol{r})$, with ζ taking values from 0 to 1. In order to avoid singularities when $\zeta \to 0$, the FEP simulations were performed using a soft-core version[24] of the Lennard-Jones potential (LJSC)

$$\mathcal{V}_{ij}^{\text{LJSC}}(r; \zeta, n, \alpha) = \zeta^n 4\epsilon_{ij}\left\{\frac{1}{[\alpha(1-\zeta)^2 + (r/\sigma_{ij})^6]^2} - \frac{1}{\alpha(1-\zeta)^2 + (r/\sigma_{ij})^6}\right\} \tag{19}$$

truncated and shifted at a cutoff radius of $r_c = 2.5\sigma$ such that $\mathcal{V}_{ij}^{\text{LJSCTS}}(r) = (\mathcal{V}_{ij}^{\text{LJSC}}(r) - \mathcal{V}_{ij}^{\text{LJSC}}(r_c))\theta(r_c - r)$ with θ being the Heaviside step function. Values of $n = 1$ and scaling constant $\alpha = 0.5$ were used. For $\zeta = 1$, Eq. 19 reduces to the standard Lennard-Jones potential, and in the limit $\zeta \to 0$ no work is required to change from $\alpha = 0$ to $0 < \alpha < \infty$ (i.e. the two potentials have equivalent initial states). Therefore, the soft-core version gives the same free energy difference as the standard LJ (or LJTS) potential.[24]

Each FEP simulation used a cubic simulation cell containing 5000 particles, and additionally the single particle being inserted. The systems were equilibrated for 20τ in the NVT ensemble, then for $2 \times 10^3\tau$ in the NPT ensemble. The particle insertion was then performed in steps of 0.01ζ over a $10^4\tau$ production run. A timestep of 0.002τ was used. Temperature (pressure) was controlled using the Nosé-Hoover chain thermostat (barostat), with 3 chains, and a time constant of 1τ (5τ). Sampling consisted of 1700-2000 replicas for μ_1^{ex}, and 500-600 replicas for μ_2^{ex}.

The chemical potentials and the derivative $(\partial\mu_1/\partial x_1)_{P,T} = (\partial\mu_1^{\text{id}}/\partial x_1)_{P,T} + (\partial\mu_1^{\text{ex}}/\partial x_1)_{P,T}$ are shown in Fig. 13. $(\partial\mu_1^{\text{id}}/\partial x_1)_{P,T}$ and $(\partial\mu_1^{\text{ex}}/\partial x_1)_{P,T}$ were evaluated at x_1 by fitting a straight line through the three points within $x_1 \pm 0.01$ and $x_1 \pm 0.05$, respectively.
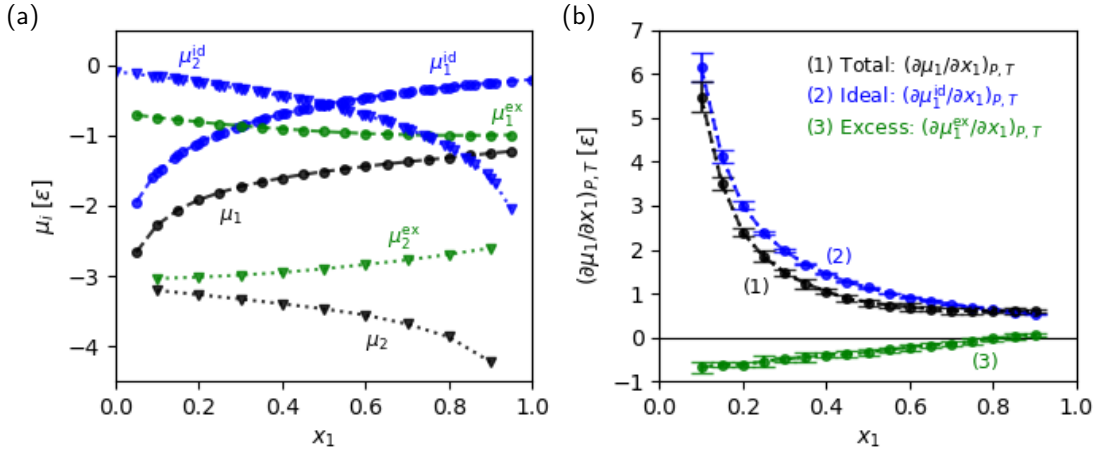
Figure 13: The chemical potential and its derivative as a function of mole fraction x_i. (a) Total μ_i, ideal μ_i^{id} and excess μ_i^{ex} chemical potentials μ_i of species $i = 1, 2$. (b) $(\partial\mu_1/\partial x_1)_{P,T}$ and its ideal and excess contributions. In (a), statistical uncertainties are smaller than the size of the symbols.

2.6 Self-diffusion coefficients and shear viscosity

The self-diffusion coefficients D_i of species $i = 1, 2$ were calculated from the average mean square displacement (MSD) using the Einstein relation

$$D_i = \frac{1}{2d}\lim_{t\to\infty}\frac{\langle|\boldsymbol{r}_i(t+t_0) - \boldsymbol{r}_i(t_0)|^2\rangle}{t} \tag{20}$$

where $\boldsymbol{r}_i$ is the position vector of a particle of species i, t is the elapsed time from arbitrary starting time t_0, and $d = 3$ is the number of spatial dimensions. D_i was therefore calculated by fitting to the equation $\langle|\boldsymbol{r}_i(t) - \boldsymbol{r}_i(0)|^2\rangle = 6tD_i$, excluding the first 10 τ of data to ensure only the diffusive regime was sampled (as opposed to the ballistic regime). In order to account for finite-size effects, the "infinite-size" diffusion coefficient $D_{i,0}$ was calculated by extrapolation to $L^{-1} = 0$, where L is the length of the cubic simulation cell. This finite-size analysis is shown in Fig. 14, and follows from the equation derived by Yeh and Hummer[25] using a simple hydrodynamic model of a particle surrounded by a solvent of viscosity η_{YH} in a periodically replicated simulation cell,

$$D_{i,\text{PBC}} = -\frac{\xi k_{\text{B}}T}{6\pi\eta_{\text{YH}}}L^{-1} + D_{i,0} \tag{21}$$

where $D_{i,\text{PBC}}$ are the finite-size diffusion coefficients calculated from our MD simulations, and ξ is a dimensionless constant equal to 2.837297 for a cubic simulation cell with 3D periodic boundary
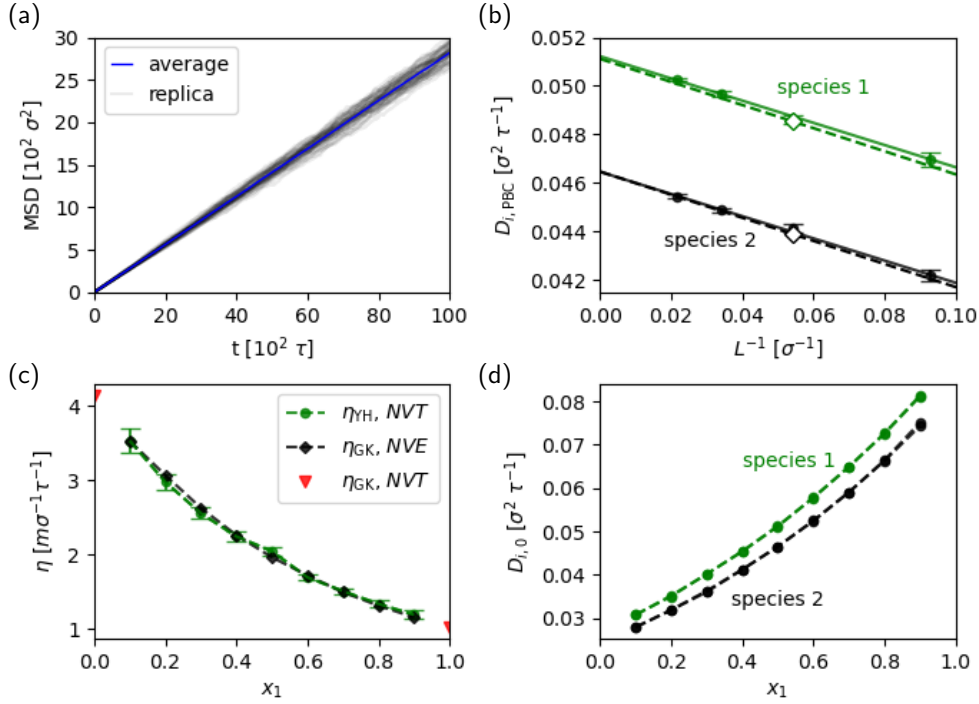
Figure 14: Self-diffusion coefficients and shear viscosities of the Lennard-Jones mixtures. (a) Mean-square displacement (MSD) *vs.* time t for the $x_1 = 0.5$ and $N = 1000$ system. (b) Finite-size analysis for the $x_1 = 0.5$ mixture: $D_{i,\mathrm{PBC}}$ is the finite-size diffusion coefficient of species i and L is the length of the cubic simulation cell. Symbols: circles ($\circ$) and diamonds ($\diamond$) show the data from NVT and NVE MD simulations, respectively. Solid lines show a linear fit to the NVT data; dashed lines show a straight line through the single NVE data point with the gradient determined from η_{GK}. (c) The viscosities η as a function of mole fraction x_1, as determined from the different methods (see main text). (d) "Infinite-size" diffusion coefficients $D_{i,0}$ of species i as a function of x_1. $D_{i,0}$ from the two methods, NVT simulations with direct extrapolation (η_{YH}) and NVE simulations with η_{GK}, cannot be distinguished on the scale of the plot. Where error bars are not explicitly shown, the statistical uncertainty is smaller than the size of the symbol.

conditions.[25] The same expression was obtained earlier[26] by Dünweg and Kremer using a closely related derivation. For each state point, the $i = 1$ and $i = 2$ data sets were simultaneously fit to Eq. 21, giving a single viscosity η_{YH} for the mixture.

The shear viscosity η was additionally calculated using the Green-Kubo integral formula

$$\eta_{GK} = \frac{V}{k_{\mathrm{B}}T} \lim_{t' \to \infty} \int_0^{t'} \langle P_{\alpha\beta}(t)P_{\alpha\beta}(0)\rangle dt \tag{22}$$
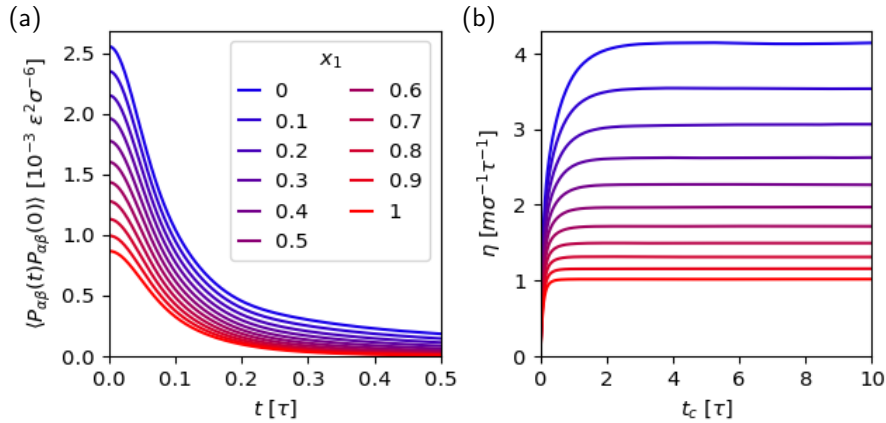
20

Figure 15: (a) Autocorrelation functions $\langle P_{\alpha\beta}(t)P_{\alpha\beta}(0)\rangle$ as a function of time lag t. (b) Convergence of shear viscosity $\eta(t_c)$ with the correlation time t_c used as the upper limit of the integral in Eq. 22.

where $\alpha \neq \beta$ such that $P_{\alpha\beta}$ are the off-diagonal elements of the pressure tensor. Results were averaged over $(\alpha, \beta) = (x, y)$, (x, z) and (y, z). A correlation time of $t_c = 10\tau$ was used for the upper limit of the integral, which is sufficient to obtain well-converged integrals (see Fig. 15).

In order to accurately target a specific thermodynamic states when calculating $D_{i,\mathrm{PBC}}$, the NVT ensemble was sampled using a temperature-control algorithm that alters dynamics compared to the Newtonian dynamics of the NVE ensemble. It is therefore necessary to check whether the employed global Nosé–Hoover (three chains) thermostat affects the computed self-diffusion coefficients. We show in Fig. 14(b)&(c) that it does not: all diffusion coefficients and viscosities calculated from NVT and NVE simulations, and using the different methods (Eqs. 21&22) agree to within their associated uncertainties. This is consistent with previous work that shows that "global" velocity scaling thermostats, including the Nosé–Hoover-chain thermostat, do not significantly alter diffusion coefficients or viscosity.[27,28]

2.7 Kirkwood-Buff integrals from grand canonical Monte Carlo

KBIs were calculated from grand canonical Monte Carlo simulations. For each simulation, the temperature of the ideal gas reservoir was set to $T = 0.62 \ \epsilon k_B^{-1}$, and the input chemical potentials μ_1 and μ_2 were determined from the free-energy perturbation simulations described in Sec. 2.5. In all cases, a cubic simulation cell with length $L = 20\sigma$ was used. Each MC step, 100 trial displacement and 100 trial exchanges (insertions or deletions with equal probability) were attempted. For the displacement moves, a maximum translation distance of 1.0σ was allowed.

Trial moves were accepted/rejected using the standard Metropolis criterion. Each replica was first equilibrated in an NVT MD simulation at the target x_1 and ρ_N for 200 τ, followed by 10^5 MC steps, and finally a production run of 10^7 MC steps. Sampling consisted of 400-500 statistically independent replicas for each state point.

The Kirkwood-Buff integrals G_{ij} were calculated from the particle number fluctuations according to

$$G_{ij} = V \frac{\langle N_i N_j \rangle - \langle N_i \rangle \langle N_j \rangle}{\langle N_i \rangle \langle N_j \rangle} - V \frac{\delta_{ij}}{\langle N_j \rangle} \tag{23}$$

where N_i is the number of particles of species i and V is the volume of the simulation cell. The average pressures are within $\pm 0.008 \epsilon \sigma^{-3}$ of $P = 0.46$ $\epsilon \sigma^{-3}$, corresponding to differences in number density on the order of $\delta \rho_N \sim 10^{-4} \sigma^{-3}$ relative to those calculated from NPT MD simulations (see Fig. 1(a)). Differences in G_{ij} and subsequently Γ due to the slightly different thermodynamic states being sampled are expected to be insignificant compared to their associated statistical uncertainties.

2.8 Kirkwood-Buff integrals from molecular dynamics (NVT) simulations

For an infinitely large and open three-dimensional system, the KBI for mixture components i and j is defined as

$$G_{ij} = 4\pi \int_0^\infty [g_{ij}^{\mu VT}(r) - 1] r^2 dr \tag{24}$$

where r is the radial distance between particles i and j. The infinite-size KBIs were calculated from a finite-size analysis of finite-volume KBIs

$$G_{ij}^V = \int_V [g_{ij}^{\mu VT}(r) - 1] w(r) dr \tag{25}$$

defined for finite and open subvolumes embedded in a reservoir.[29] For spherical symmetry $w(r) = 4\pi r^2 (1 - 3x/2 + x^3/2)$ valid for $x < 1$, where $x = r/(2R)$ and R is the radius of the subvolume. $g_{ij}^{\mu VT}$ is the pair correlation function *in the thermodynamic limit*. It has been shown that G_{ij}^V scales linearly with R^{-1} and that the infinite-size G_{ij} can be obtained by extrapolating the linear regime to $R^{-1} = 0$.[29–31]

We calculate the RDFs from simulations of $N = 10^5$ to $N = 5 \times 10^6$ particles in the NVT ensemble. Because fluctuations transform between ensembles, $g_{ij}^{\mu VT}$ cannot be formally replaced with g_{ij}^{NVT}. However, for a sufficiently large system, the correlation lengths of particle density
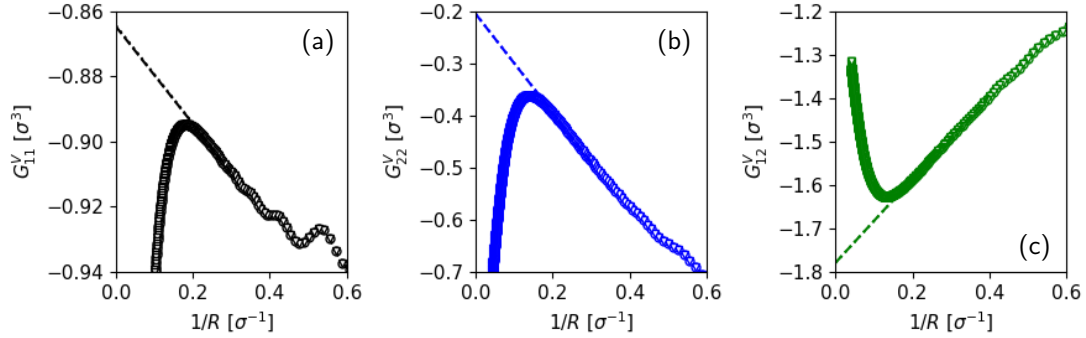
Figure 16: Extrapolation of the finite-volume Kirkwood-Buff integrals G_{ij}^V to $R^{-1} = 0$, where R is the radius of the subvolume: (a) G_{11}^V, (b) G_{22}^V and (c) G_{12}^V. The data shown corresponds to mole fraction $x_1 = 0.5$ and a system size of $N = 5 \times 10^6$ particles. Symbols: circles $(\cdots \circ \cdots)$ and downward triangles $(\cdots \triangledown \cdots)$ denote the use of pair correlation function g_{ij} (uncorrected) and the corrected g_{ij}^{GV}, respectively, although these cannot be easily distinguished on the scale of the plots.

fluctuations are small compared to the linear dimension of the simulation cell, and local correlations are expected to be well reproduced. In addition to a large system size, we apply the tail correction[31] of Ganguly and van der Vegt to ensure the correct asymptotic limit ($\lim_{r \to \infty} g_{ij} = 1$) of the RDF.

$$g_{ij}^{GV}(r) = g_{ij}(r) \left(\frac{N_j h(r)}{N_j h(r) - n_{ij}^{ex}(r) - \delta_{ij}} \right) \qquad (26)$$

$$h(r) = 1 - \frac{4\pi r^3}{3V} \qquad (27)$$

where N_j is the total number of particles j in the simulation cell of volume V. However, we note that in our simulations, this correction does not have an appreciable effect on the linear regime and subsequently the extrapolated G_{ij} (see Fig. 16). Other corrections[32,33] to the RDFs for calculating KBIs have been proposed; the correction of Ganguly and van der Vegt was found to be the most accurate for a WCA system, relative to a larger reference system ($L = 80\sigma$).[30]

We show in Fig. 17 a finite-size analysis of the infinite-size KBIs. The final values for G_{ij} in the main text were taken from the largest system size, and the associated uncertainties were estimated from the convergence with system size.
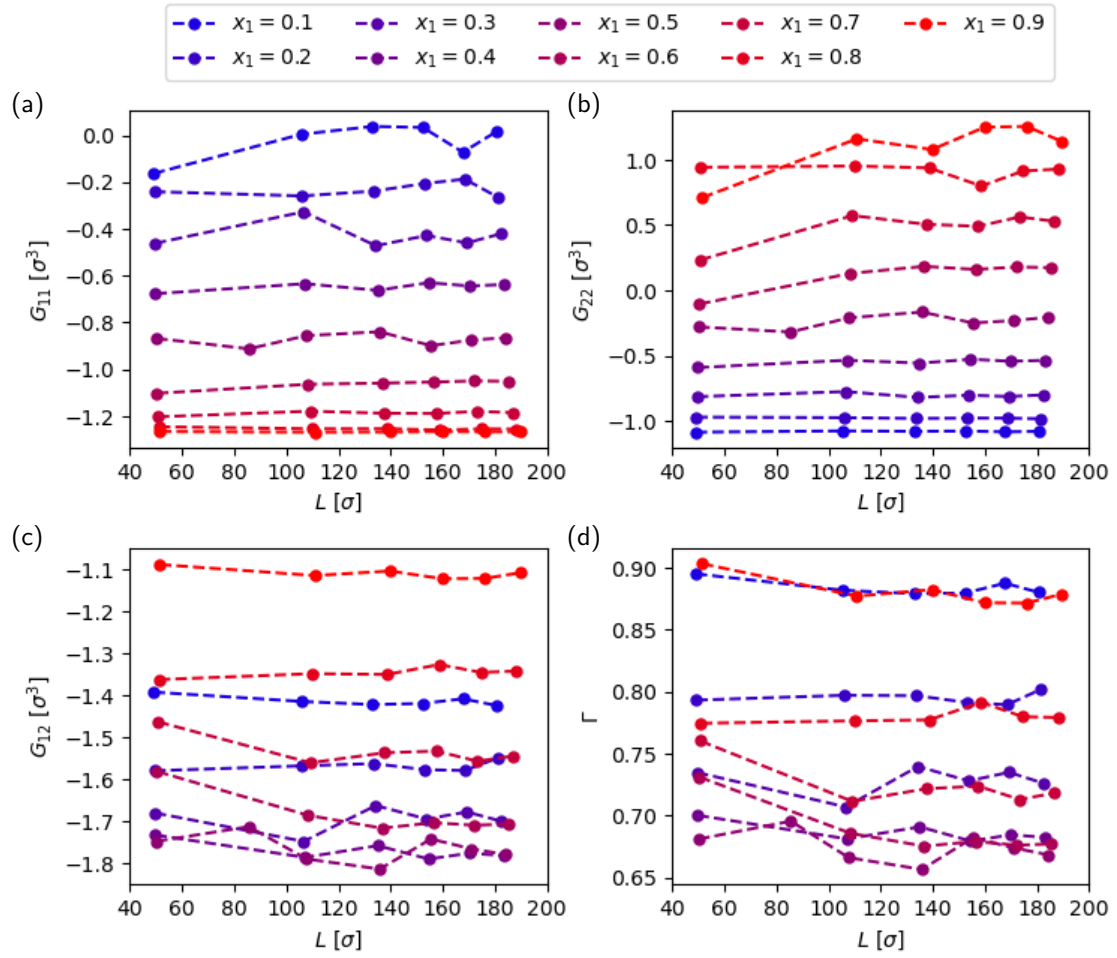
23

Figure 17: Finite-size analysis of the infinite-size Kirkwood-Buff integrals G_{ij} as a function of simulation cell length L, for different mole fractions x_1. (a) G_{11}, (b) G_{22}, (c) G_{12}, and (d) thermodynamic factor Γ.

2.9 Melting points of the pure components

The melting temperatures T_m of the pure components $i = 1, 2$ were determined using the direct coexistence method in the NP_zT ensemble. This involves preparing a solid-liquid interface at a given (T, P) state point and observing whether the system completely melts, freezes, or remains in coexistence. In MD simulations, cooling a homogeneous liquid below its melting point usually results in a metastable supercooled liquid; freezing is not observed unless prohibitively long simulations are performed. Likewise, heating a solid slightly above its melting point results in a superheated solid. The presence of the interface lowers the kinetic barrier for melting/freezing.

24

First, the densities of the solid and liquid phases were determined from NPT simulations. Initial configurations were prepared by joining two half-boxes, one of the FCC-solid the other of the liquid, each containing $N = 5324$ particles and equilibrated in the NVT ensemble. The combined $N = 10648$ system was then equilibrated for 20τ, ensuring that the solid phase did not melt by restraining each solid particle to its equilibrium position $\boldsymbol{r}_0$ with a harmonic potential, $\mathcal{V}(\boldsymbol{r}) = k(\boldsymbol{r} - \boldsymbol{r_0})^2/2$ of force constant $k = 10 \ \epsilon\sigma^{-2}$. A $4 \times 10^4\tau$ production run in the NP_zT ensemble was then performed, applying a barostat only to the direction parallel to the surface normal (the z-direction). A Nosé-Hoover chain barostat was used, with 3 chains, and a time constant of $4 \ \tau$. Likewise, a Nosé-Hoover chain thermostat was used, also with 3 chains, and a time constant of $1 \ \tau$. Sampling consisted of an initial 10 statistically independent replicas, followed by an additional 40 replicas if the initial set did not all either melt or freeze. In all cases, a homogeneous phase was observed by the end of the production run.

The simulations were performed in the NP_zT ensemble, and as such the simulation cell dimensions (L_x and L_y) were chosen to be consistent with the density of the solid at the (T, P) state point. Otherwise, the solid phase would possess internal stress,[34,35] corresponding to a higher free energy, and resulting in the overestimation of the coexistence pressure and/or underestimation of the melting temperature.

Each replica was determined to have either frozen or melted using the Q_6 ($l = 6$) bond-orientational order parameter. The Steinhardt order parameters Q_l were introduced to characterize local orientational order in atomic structures,[36] and are given by

$$Q_l = \sqrt{\frac{4\pi}{2l+1} \sum_{m=-l}^{+l} \bar{Y}_{lm} \bar{Y}_{lm}^*} \qquad (28)$$

$$\bar{Y}_{lm} = \frac{1}{N_n} \sum_{j=1}^{N_n} Y_{lm}(\theta(\boldsymbol{r}_{ij}), \phi(\boldsymbol{r}_{ij})) \qquad (29)$$

for each particle i, where $Y_{lm}(\theta, \phi)$ are the spherical harmonics, θ and ϕ are the polar angles of "bond" vector $\boldsymbol{r}_{ij}$ between i and neighbour j, and N_n is the number of nearest neighbours to particle i. Q_l is therefore a rotationally invariant non-negative amplitude. Q_l adopt well-defined values for high-symmetry structures; for a perfect FCC crystal ($Fm\bar{3}m$) and $N_n = 12$, $Q_6 = 0.575$.[37] We show in Fig. 18 that the Q_6 order parameter can be used to distinguish between the FCC solid and liquid phases. The replica was determined to have frozen if $\langle Q_6 \rangle > 0.496$, or melted if $\langle Q_6 \rangle < 0.375$. The average $\langle Q_6 \rangle$ was taken over the last $10 \ \tau$ of the trajectory.

In the thermodynamic limit, a solid melts at $T > T_m$, and a liquid freezes for $T < T_m$. However, a finite-size system may stochastically melt or freeze with probabilities P_m and $P_f =$
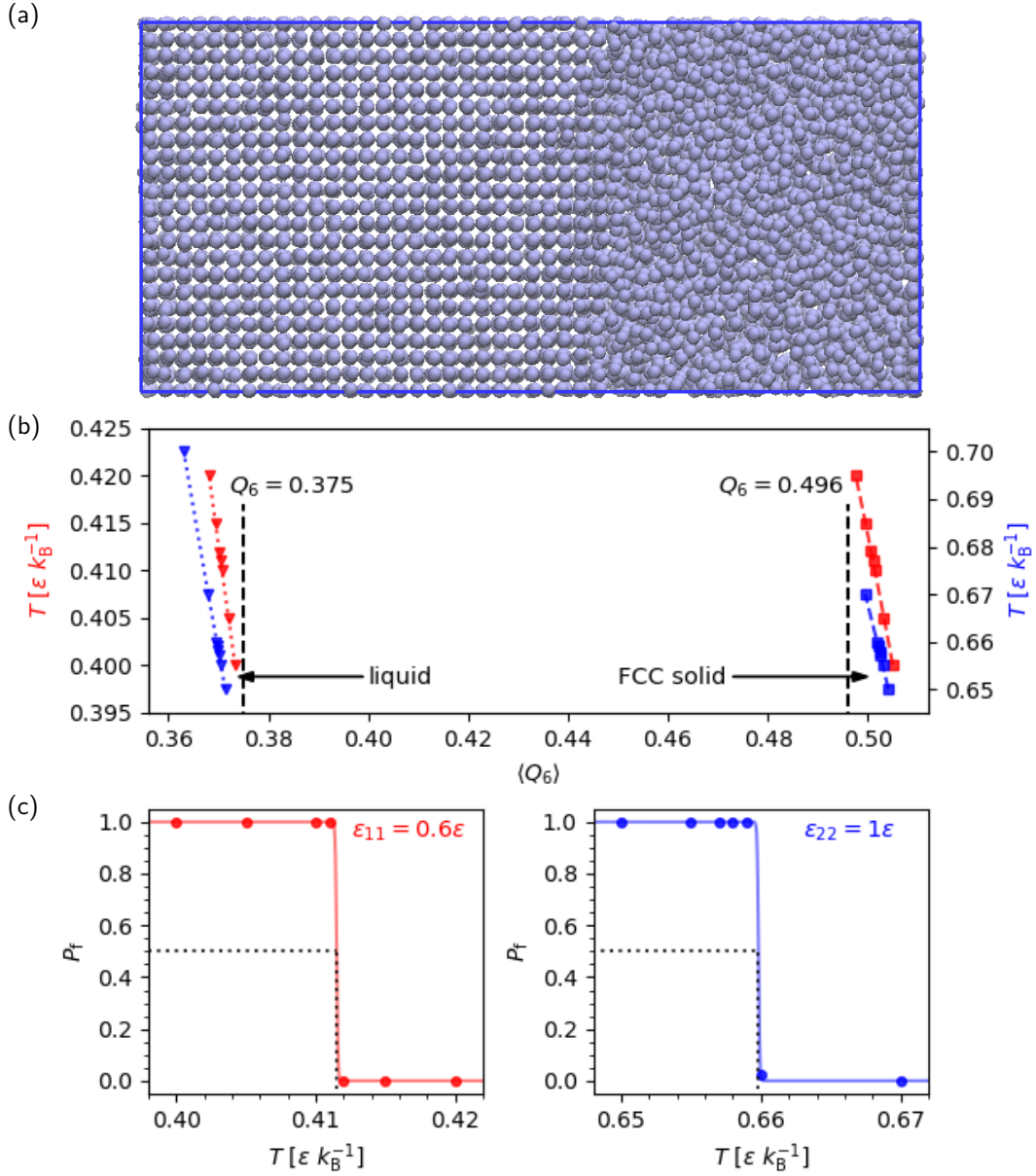
Figure 18: Melting points of the pure components determined using the direct coexistence method. (a) Snapshot of the simulation cell in the process of melting/freezing. (b) Lennard-Jones liquids and FCC solids at temperatures T characterized by their average Q_6 order parameter. Species 1 (species 2) is shown in red (blue) and on the left (right) axis. (c) Probability of freezing P_f as a function of temperature T for species 1 (left) and 2 (right). Solid lines show the fitted sigmoid-like functions (Eq. 30).

$1 - P_m$ respectively. For each component, T_m was determined by fitting $P_f(T)$ to the sigmoid-like function (Fig. 18):

$$P_f(T) = \frac{1}{2} - \frac{1}{2} \tanh\left[(T - T_m)/d\right] \tag{30}$$

where d controls the sharpness of the probability profile, with $\delta_{10-90} = 2.178d$ being the width of the interval where P_f goes from 0.1 to 0.9. The melting (coexistence) temperature is defined by $P_m(T_m) = P_f(T_m) = 0.5$. The melting temperatures are shown in Table 1 alongside other coexistence properties (coexistence densities and enthalpies were determined by interpolating data from the NPT simulations).

Table 1: Solid-liquid coexistence properties of the pure LJ components at $P = 0.46\ \epsilon\sigma^{-3}$: the melting temperature T_m; coexistence number densities of the FCC solid and liquid phases, $\rho_{N,s}$ and $\rho_{N,l}$, respectively; and the enthalpy of fusion ΔH_{fus}

Species	$T_m\ [\epsilon k_{\mathrm{B}}^{-1}]$	$\rho_{N,s}\ [\sigma^{-3}]$	$\rho_{N,l}\ [\sigma^{-3}]$	$\Delta H_{\text{fus}}\ [\epsilon]$
1	0.4115(5)	0.9550(2)	0.8500(3)	0.523(3)
2	0.6598(3)	0.9509(1)	0.8419(2)	0.927(3)

References

[1] M. R. Hitchcock and C. K. Hall, "Solid–liquid phase equilibrium for binary lennard-jones mixtures", J. Chem. Phys. **110**, 11433–11444 (1999).

[2] C. Galvin, R. Grimes, and P. Burr, "A molecular dynamics method to identify the liquidus and solidus in a binary phase diagram", Comput. Mater. Sci. **186**, 110016 (2021).

[3] C. D. Thurmond, "Equilibrium thermochemistry of solid and liquid alloys of germanium and of silicon. I. the solubility of Ge and Si in elements of Groups III, IV and V", J. Phys. Chem. **57**, 827–830 (1953).

[4] R. Haase, "Zur thermodynamisch ph anomenologischen theorie der thermodiffusion", Zeitschrift f ur Physik **127**, 1–10 (1949).

[5] L. J. T. M. Kempers, "A comprehensive thermodynamic theory of the soret effect in a multicomponent gas, liquid, or solid", J. Chem. Phys. **115**, 6330–6341 (2001).

[6] K. Shukla and A. Firoozabadi, "A new model of thermal diffusion coefficients in binary hydrocarbon mixtures", Ind. Eng. Chem. Res. **37**, 3331–3342 (1998).

[7] P.-A. Artola, B. Rousseau, and G. Galliéro, "A new model for thermal diffusion: kinetic approach", J. Am. Chem. Soc. **130**, 10963–10969 (2008).

[8] E. L. Dougherty and H. G. Drickamer, "A theory of thermal diffusion in liquids", J. Chem. Phys. **23**, 295–309 (1955).

[9] E. L. Dougherty and H. G. Drickamer, "Thermal diffusion and molecular motion in liquids", J. Phys. Chem. **59**, 443–449 (1955).

[10] L. J. Tichacek, W. S. Kmak, and H. G. Drickamer, "Thermal diffusion in liquids; the effect of non-ideality and association", J. Phys. Chem. **60**, 10963–10969 (1956).

[11] M. Eslamian and M. Z. Saghir, "A critical review of thermodiffusion models: role and significance of the heat of transport and the activation energy of viscous flow", J. Non-Equilib. Thermodyn. **34**, 97–131 (2009).

[12] M. Eslamian and M. Z. Saghir, "Dynamic thermodiffusion model for binary liquid mixtures", Phys. Rev. E **80**, 011201 (2009).

[13] Y. Yan, P. Blanco, M. Z. Saghir, and M. M. Bou-Ali, "An improved theoretical model for thermal diffusion coefficient in liquid hydrocarbon mixtures: comparison between experimental and numerical results", J. Chem. Phys. **129**, 194507 (2008).

[14] S. Pan, M. Z. Saghir, M. Kawaji, C. G. Jiang, and Y. Yan, "Theoretical approach to evaluate thermodiffusion in aqueous alkanol solutions", J. Chem. Phys. **126**, 014502 (2007).

[15] P.-A. Artola and B. Rousseau, "Microscopic interpretation of a pure chemical contribution to the soret effect", Phys. Rev. Lett. **98**, 125901 (2007).

[16] Hoang, Hai and Galliero, Guillaume, "Predicting thermodiffusion in simple binary fluid mixtures", Eur. Phys. J. E **45**, 42 (2022).

[17] S. R. de Groot and P. Mazur, *Non-equilibrium thermodynamics* (Dover, 1984).

[18] N. Ohtori, Y. Ishii, Y. Togawa, T. Oono, and K. Takase, "Thermal conductivity of simple liquids: temperature and packing-fraction dependence", Phys. Rev. E **89**, 022129 (2014).

[19] J. Armstrong and F. Bresme, "Thermal conductivity of highly asymmetric binary mixtures: how important are heat/mass coupling effects?", Phys. Chem. Chem. Phys. **16**, 12307–12316 (2014).

[20] A. P. Thompson, H. M. Aktulga, R. Berger, D. S. Bolintineanu, W. M. Brown, P. S. Crozier, P. J. in 't Veld, A. Kohlmeyer, S. G. Moore, T. D. Nguyen, R. Shan, M. J. Stevens, J. Tranchida, C. Trott, and S. J. Plimpton, "LAMMPS - a flexible simulation tool for particle-based materials modeling at the atomic, meso, and continuum scales", Comp. Phys. Comm. **271**, 108171 (2022).

[21] S. H. Jamali, L. Wolff, T. M. Becker, A. Bardow, T. J. H. Vlugt, and O. A. Moultos, "Finite-size effects of binary mutual diffusion coefficients from molecular dynamics", J. Chem. Theory Comput. **14**, 2667–2677 (2018).

[22] A. T. Celebi, S. H. Jamali, A. Bardow, T. J. H. Vlugt, and O. A. Moultos, "Finite-size effects of diffusion coefficients computed from molecular dynamics: a review of what we have learned so far", Mol. Simul. **47**, 831–845 (2021).

[23] N. A. T. Miller, P. J. Daivis, I. K. Snook, and B. D. Todd, "Computation of thermodynamic and transport properties to predict thermophoretic effects in an argon-krypton mixture", J. Chem. Phys. **139**, 144504 (2013).

[24] T. C. Beutler, A. E. Mark, R. C. van Schaik, P. R. Gerber, and W. F. van Gunsteren, "Avoiding singularities and numerical instabilities in free energy calculations based on molecular simulations", Chem. Phys. Lett. **222**, 529–539 (1994).

[25] I.-C. Yeh and G. Hummer, "System-size dependence of diffusion coefficients and viscosities from molecular dynamics simulations with periodic boundary conditions", J. Phys. Chem. B **108**, 15873–15879 (2004).

[26]B. Dünweg and K. Kremer, "Molecular dynamics simulation of a polymer chain in solution", J. Chem. Phys. **99**, 6983–6997 (1993).

[27]J. E. Basconi and M. R. Shirts, "Effects of temperature control algorithms on transport properties and kinetics in molecular dynamics simulations", J. Chem. Theory Comput. **9**, 2887–2899 (2013).

[28]O. R. Gittus and F. Bresme, "Thermophysical properties of water using reactive force fields", J. Chem. Phys. **155**, 114501 (2021).

[29]P. Krüger, S. K. Schnell, D. Bedeaux, S. Kjelstrup, T. J. H. Vlugt, and J.-M. Simon, "Kirkwood–buff integrals for finite volumes", J. Phys. Chem. Lett. **4**, 235–238 (2013).

[30]N. Dawass, P. Krüger, S. K. Schnell, D. Bedeaux, S. Kjelstrup, J. M. Simon, and T. J. H. Vlugt, "Finite-size effects of kirkwood–buff integrals from molecular simulations", Mol. Simul. **44**, 599–612 (2018).

[31]P. Ganguly and N. F. A. van der Vegt, "Convergence of sampling kirkwood–buff integrals of aqueous solutions with molecular dynamics simulations", J. Chem. Theory Comput. **9**, 1347–1355 (2013).

[32]J. J. Salacuse, A. R. Denton, and P. A. Egelstaff, "Finite-size effects in molecular dynamics simulations: static structure factor and compressibility. i. theoretical method", Phys. Rev. E **53**, 2382–2389 (1996).

[33]R. Cortes-Huerto, K. Kremer, and R. Potestio, "Communication: kirkwood-buff integrals in the thermodynamic limit from small-sized molecular dynamics simulations", J. Chem. Phys. **145**, 141103 (2016).

[34]J. R. Espinosa, E. Sanz, C. Valeriani, and C. Vega, "On fluid-solid direct coexistence simulations: the pseudo-hard sphere model", J. Chem. Phys. **139**, 144502 (2013).

[35]D. Frenkel, "Simulations: the dark side", Eur. Phys. J. Plus **128**, 1–21 (2013).

[36]P. J. Steinhardt, D. R. Nelson, and M. Ronchetti, "Bond-orientational order in liquids and glasses", Phys. Rev. B **28**, 784–805 (1983).

[37]W. Mickel, S. C. Kapfer, G. E. Schröder-Turk, and K. Mecke, "Shortcomings of the bond orientational order parameters for the analysis of disordered particulate matter", J. Chem. Phys. **138**, 044501 (2013).